Operando focused ion beam–scanning electron microscope (FIB-SEM) revealing microstructural and morphological evolution in a solid-state battery

Patrice Perrenot, Pascale Bayle-Guillemaud, Pierre-Henri Jouneau, Adrien Boulineau, Claire Villevieille

Operando Focused Ion Beam – Scanning electron microscope (FIB-SEM) revealing microstructural and morphological evolution in solid-state battery

Patrice Perrenot[1], Pascale Bayle-Guillemaud[2], Pierre-Henri Jouneau[1], Adrien Boulineau[1], Claire Villevieille[3*]*

1 Université Grenoble Alpes, CEA, Liten, DTNM, 38000 Grenoble, France

2 Université Grenoble Alpes, CEA, IRIG, 38000 Grenoble, France

3 Université Grenoble Alpes, Univ. Savoie Mont Blanc, CNRS, Grenoble INP, LEPMI, 38000 Grenoble, France

AUTHOR INFORMATION

Corresponding Author

* E-mail: adrien.boulineau@cea.fr; claire.villevieille@grenoble-inp.fr

ABSTRACT

Thiophosphates have emerged as a promising solid electrolyte for the forthcoming solid-state battery technology if one can control the transport properties both electronic and ionic within the composite electrode. Unfortunately, during cycling, several chemo-mechanical degradations are occurring hindering the transport properties inside the batteries. Solutions could be provided if one could track the dynamics of such degradation processes. The development of a specific *operando* focused ion beam – scanning electron microscope (FIB-SEM) approach helps us to perform imaging during cycling and thus address the dynamic morphological investigation of a composite electrode $LiNi_{0.6}Mn_{0.2}Co_{0.2}O_2$ (NMC622 couple to amorphous Li_3PS_4). This new methodology makes it possible to highlight mechanical stress endured by the electroactive materials and by the electrolyte during cycling. In this study, polycrystalline NMC622 microstructural evolution was monitored during charge and discharge, showing that the polycrystalline morphology is poorly adapted to solid-state batteries and that the interface adhesion should be better controlled to enhance electrochemical performance.

TOC GRAPHICS

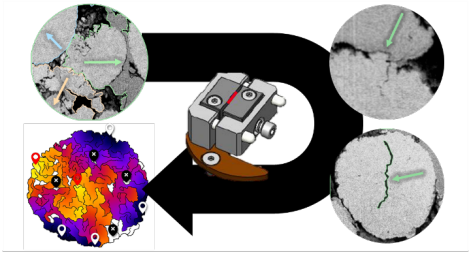

Solid-state batteries are believed to be the next breakthrough in electrochemical energy storage systems if one can control their chemo-mechanical degradations [1–3]. Different solid electrolytes are under investigation but sulfide ones stand out in the category[4–6]. However, the main difficulties in solid-state batteries rely on the transport properties, both ionic and electronic, within the composite electrode which can only be achieved thanks to intimate contact between the electroactive materials and the solid electrolyte. If one can control the intimate contact before cycling, unfortunately during cycling, the electroactive materials are breathing, due to Li intercalation processes, causing mechanical fracture and microstructural changes including interfacial contact loss[7]. LPS-family (Li_2S-P_2S_5) could help to buffer the breathing processes since its elastic limits are favourable and could help maintain the composite electrolyte cohesion during cycling[8,9]. As high energy density is targeted in solid-state batteries, NMC layer oxide materials should be a material of choice, nevertheless, it suffers some volume changes (4.4 % at 4.2 V vs Li^+/Li[10,11]) during cycling: an increase of the c-axis lattice parameter with a decrease of the a-axis parameter causes mechanical stress on the secondary particles. This type of mechanical distortion on the active materials coupled to the sintering of the composite electrode can cause severe battery failure on solid-state batteries where microstructure plays a key role. Recently, FIB-SEM tomography has played a key role in revealing the battery microstructure of materials and interfaces[12,13]. Shi *et al*. reported an increase of porosity in the composite positive electrode, most likely arising from decohesion from NMC532 and amorphous LPS[14]. However, most of these investigations are carried out using *ex situ* samples where the microstructure might have been influenced by i) the cell relaxation (time between the cell was stopped and the sample analysed) ii) the dismounting of the cell that can cause additional microstructure evolution and/or iii) air/moisture exposure or other type of contamination that could change the real fate of the samples. Yadav *et al*. investigated the degradation mechanism at LPS and Li metal interface[15] using an *in*

situ SEM approach but only surfaces of the cell stack could be investigated. Alternatively, large-scale facilities on the other hand such as X-Ray Computed Tomography enable the *operando* investigation of the bulk microstructure of the battery[16,17]. Unfortunately, several challenges remain when using large-scale facilities: i) access to the beam is not granted and sometimes difficult to get, ii) developing specific cells is difficult due to the beam geometry, iii) to date the best resolution to be achieved by XRD-CT is 300 nm, down to 25 nm for X-ray holotomography and ptychography beam, which makes the investigation of the interfaces extremely difficult. On the other side, FIB-SEM can be a complementary technique when it comes to surface/interface investigation since it offers an optimal resolution at the nanometer scale, below 25 nm, giving tremendous information about the interface processes and if carried out in an *in situ* manner, it can reveal precious localized information about single particle behavior[18–20].

In this paper, we introduce a dedicated electrochemical cell specifically designed to perform *operando* FIB-SEM measurement and allow high-resolution, dynamic morphology analysis of bulk materials (LPS coupled to NMC622). The results reveal the morphological evolution of NMC within the composite positive electrode. Indeed, the fracturing of the NMC has been observed through cycling. Moreover, due to the high tortuosity of the electrode, a lithiation/delithiation front has been observed between NMC close to the separator and close to the current collector. In addition, due to the volume shrinkage of NMC during delithiation, decohesions have been observed between the LPS and the NMC. Unfortunately, it is shown that the volume expansion during lithiation of NMC does not necessarily invert the phenomenon. Both internal fracturings of NMC and LPS-NMC decohesion will impact the electrochemical properties as the ionic/electronic pathways will be lengthened.

First, the cell needs to be designed following main criteria i) the electrochemical performance should be similar to the one obtained in the conventional cell, ii) the cell should be properly air and moisture-tight and, iii) the cell should be easily adapted to the FIB-SEM holder with cabling allowing connection to the cycling device. The solid-state cell and the *operando* cell had to be developed together. The first cell was modified from a homemade design presented in **Note 1** and **Figure S1** in Supporting Information. The second is designed within a transfer box, and its characterization is presented in **Note 2** and **Figure S2** in Supporting Information.

When preliminarily imaging the sample with the SEM, a variation of OCV of ca. 0.1 V (**Figure S2a**) is observed. This variation is fairly low and could be assigned to stress relaxation within our setup. While digging the trench with the FIB on the battery stack to reveal an optimal cross-section to be further investigated during cycling, we noticed a variation of OCV of ca. 0.2 V (from ca. 1.9 to 1.7 V vs Li^+/Li), most probably coming from charges induced by the ion beam. This OCV variation is not neglectable, and we will reduce the use of the FIB during cycling to not disturb the electrochemical processes and measurements. The pristine surface is presented in **Figure S2e**. From the primary observation, the interface between the solid electrolyte and the composite electrode is hardly visible, indicating optimal contact during shaping as demonstrated previously[6,7]. Image analyses obtained from the cross-section reveal a surface fraction of 39.6 % for NMC, 38.6 % for LPS and 21.8 % for porosity which is in agreement with our previous investigation[7]. The overall cross-section of the cell stack is presented in **Figure S3**. The pristine electrochemical characterizations are presented in **Figure S2a,b** while the cycling is presented in **Figure S4** in Supporting Information).

The beam damage related to the imaging will not be presented in the core of this letter but is addressed in Supplementary information in **Note 3**, **Figure S5** and in **Figure S6**.

The main advantage of the *operando* measurements is that multiple pieces of information can be extracted simultaneously once focusing on the composite electrode, the evolution of the electroactive materials side (NMC particles fracturing) and the interfacial contact between NMC particle and LPS.

As already demonstrated[7], the polycrystalline particles of NMC622 fracture during the shaping of the cell components. Then, during the first charge (i.e. delithiation), particles that were intact before starting cycling begin to fracture along the multiple grain boundaries caused by the overall volume shrinkage of the NMC622[21–24] as shown in **Figure 1b**, **c**. This type of fracture has already been observed in Li-rich NMC positive electrode materials by X-ray ptychography technique, and their extent was found about the size of the particles[25].

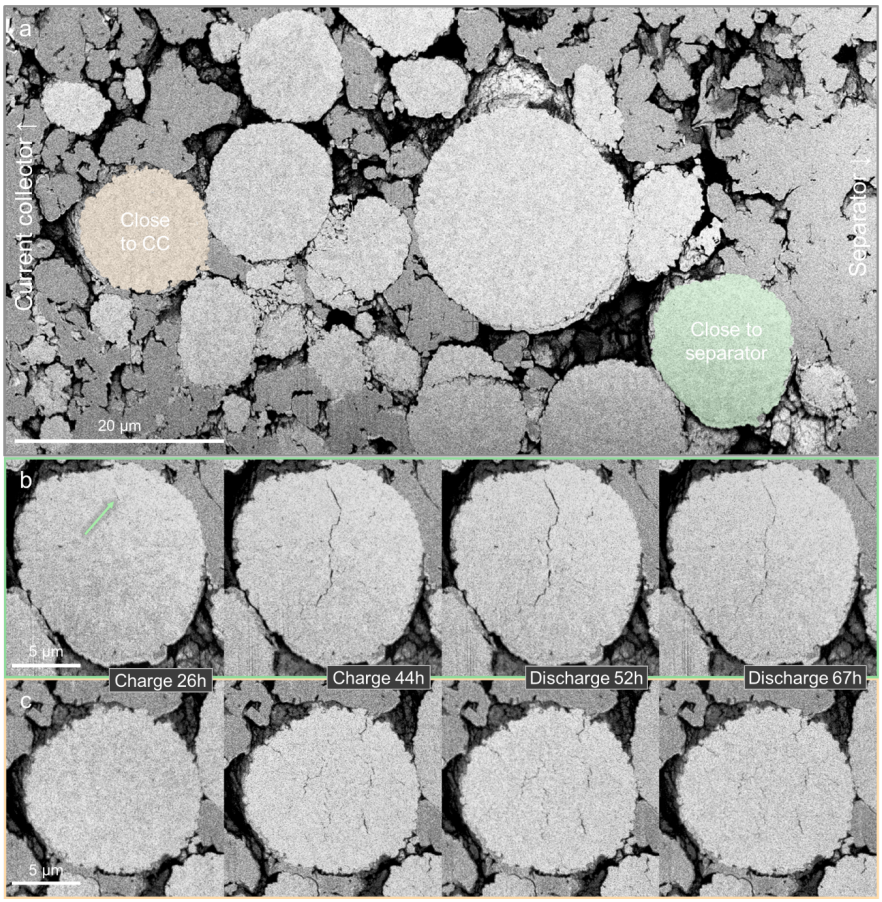

Figure 1. a) Backscattered image of the wide field cross-section view with followed NMCs highlighted at the pristine state. b-c) Backscattered images of two NMC622 particles at various time stamps highlighting the fractures during cycling, b) NMC located close to the separator side (**Movie 1 NMC fracturing**) and c) NMC located at ca. 50 µm close to the current collector side (**Movie 2 NMC fracturing and NMC-LPS decohesion**). The green arrow indicates the initiation of the fracture.

As we can follow the delithiation dynamics, we noticed a delithiation front across the positive electrode arising from a poor ionic percolation caused by the high tortuosity[7]. Indeed, the NMC particles close to the separator (**Figure 1b**) show a visible fracture at ca. 26 h (eq. to ca. 76 % of SOC) while on the NMC particles far from the separator (**Figure 1c**), the fractures only appear visible at the end of the potentiostatic plateau (44 h, eq. to ca. 99 % of SOC). The former indicates that the ionic pathway is short since, close to the separator (source of Li), the NMC is first delithiated, whereas, close to the current collector, the delithiation did not even start creating a Li gradient in the composite electrode as observed elsewhere[26]. Moreover, the effect of the size of the particle is alleviated as the two particles compared here are roughly the same diameter.

We can also note that some particles do not suffer any fracture during cycling which can be explained by i) the particles are disconnected from the electronic and ionic network, as expected by the poor electrode engineering, and/or ii) the particles are connected but not visible in the images, meaning that only a side of the particle is connected to the conductive networks, leading to internal Li gradient invisible by SEM images, iii) tougher grain boundaries between primary particles in the NMC particle, and/or iv) different lithium stoichiometry within the NMC particles. The last two formers' hypotheses are unlikely since the powder is purchased and XRD shows the signature of NMC622, also the intact particle did not fracture during the room temperature sintering process indicating that the NMC particles were not in contact between themselves, thus, most probably they are not connected to any electronic network (since no carbon additive is used). It appears that hypothesis i) is the most likely considering the amount of porosity in the positive electrode, the limited LPS-NMC connection and the low stack pressure.

During the lithiation of the NMC (i.e. discharge), the volume of the particle increases, leading to a peculiar behaviour as the gap induced by the internal fracturing is partially recovered. This behaviour is, at first, counterintuitive since the particles are again undergoing anisotropic

volume changes. The fractures could have expanded but it appears that the gap is partially recovered, and no new fractures appear. From the comparison of those two NMCs at different locations in the positive electrode, it appears that the fracturing is more drastic in particles close to the separator, indicating a deeper delithiation. In **Figure 1b** (NMC located at the separator), a fracture as wide as ca. 120 nm is formed during the charge. This fracture has a length of roughly 9 µm, crossing two-thirds of the particle and is being partially recovered at the end of the discharge (still visible with a pixel size of 42.5 nm). In **Figure 1c** (NMC located at ca. 50 µm from the separator), few fractures almost recover (fracture widths become smaller than the pixel size of 42.5 nm) but the majority remain as shown on the close-up image with a smaller pixel size (13 nm) at the end of the discharge (**Figure S7**). Here again, it appears that the NMC particles close to the separator better reduce the gap induced by the fracturing than the NMC particles far from the separator (the causes of the NMC fracture dynamics are further discussed in **Note 4**).

During the first charge, we saw that the NMC particles are fracturing internally, which can lead to a poor solid-state diffusion inside the NMC particles hindering the rate capability of the cell. It is expected that after a couple of cycles, a full disconnecting from the electronic and ionic network could occur as demonstrated in our previous study[7]. Indeed, as LPS does not cover fully the NMC particles, the path length of lithium inside the NMC will be drastically lengthened if not ruptured. When this happens not only locally but everywhere in the composite electrode, the polarization of the cell will increase as well as the electrochemical performance will decrease.

To maintain the battery performance, the LPS matrix surrounding the NMC particles must then locally adapt to the volume changes of the electroactive particles. Unfortunately, along the first charge, we can notice the decohesion of the NMC particles from the LPS matrix at the interfacial contact, as shown in Figure 23.

a supprimé: Figure 3

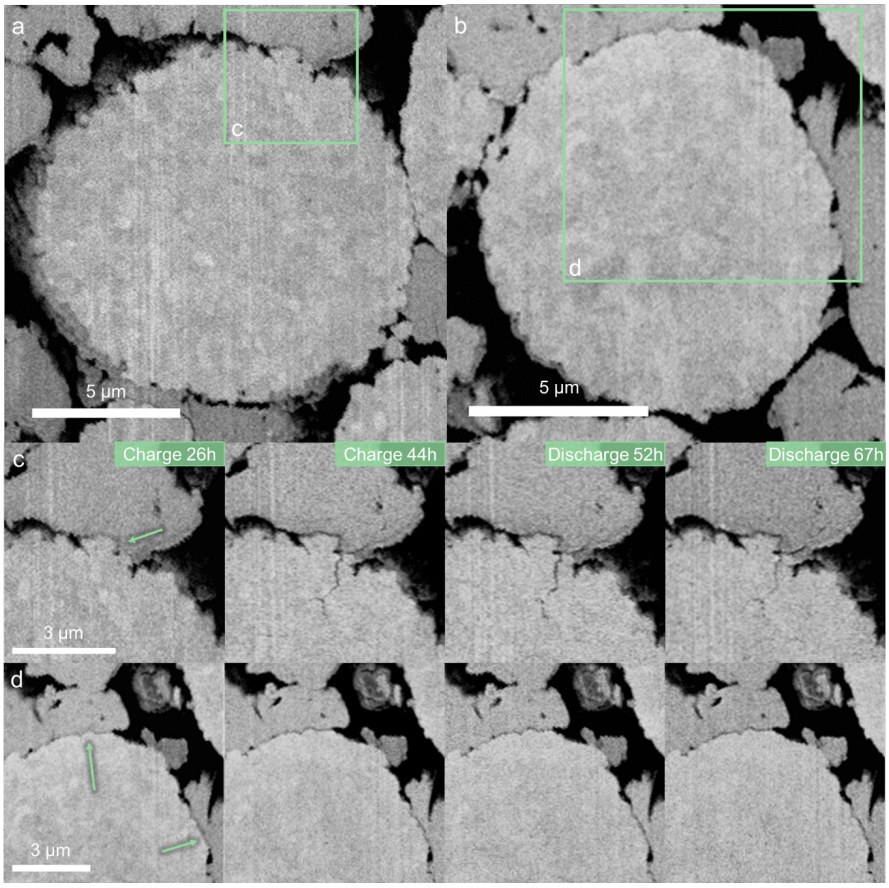

Figure 2, a and b) Secondary electron images of entire NMC particle and c and d) close-ups of NMC/LPS interfaces at various time stamps highlighting the decohesion between NMC and LPS (**Movie 2 NMC fracturing and NMC-LPS decohesion** & **Movie 3 NMC-LPS decohesion** respectively). The green arrows indicate the interface where evolution is observed.

a supprimé: 3

This decohesion process is less obvious to monitor due to its nanometric dimension but appears at the end of the charge due to the NMC volume shrinkage and is still present at the end of the discharge despite the lithiation of the NMC. During the delithiation, the volume shrinkage of

NMC leaves an imprint on the LPS matrix, the gap between the NMC particles and the LPS matrix is ca. 40 nm, sufficient to locally hinder the ionic/electronic transport properties at the interface. However, at this stage, the images are just displaying a 2D vision, and a part of the particles might be still connected but not in the field of view. On the other side during lithiation, the contact appears to be lost permanently as a gap is still visible at the end of the discharge. Higher resolution of this decohesion process can be found in Supporting Information, **Figure S8**.

As the decohesion processes are observed in 2D, this does not mean that this decohesion is always homogeneous around the particles. Some LPS-NMC connections remain within the composite, confirmed by the electrochemical cycling of the cell. Nevertheless, considering the limited observed contact of NMC with the LPS shown in Figure 23**a, b** (supported in the previous study with $\%coverage_{NMC}$ calculated at 75 % and 25 % at the pristine and charged state respectively[7]), the path of lithium inside the particles will be impacted. If considering the cross-section of NMC as the path of lithium-ion diffusion inside the particle from the LPS matrix, a geodesic distance map can show the change of pathways with a perfect case (pristine with no fractures, no decohesion, Figure 34**a**), after a first cycle (from the *operando* observation, including fractures and decohesion, Figure 34**b**) and after simulated prolonged cycling where fracturing extends (based on the same particle, including extended fracture along grain boundaries and decohesion, Figure 34**c**). **Figure S9** illustrates the principle of the calculation with the morphological evolution while cycling.

a supprimé: Figure 3

a supprimé: Figure 4

a supprimé: Figure 4

a supprimé: Figure 4

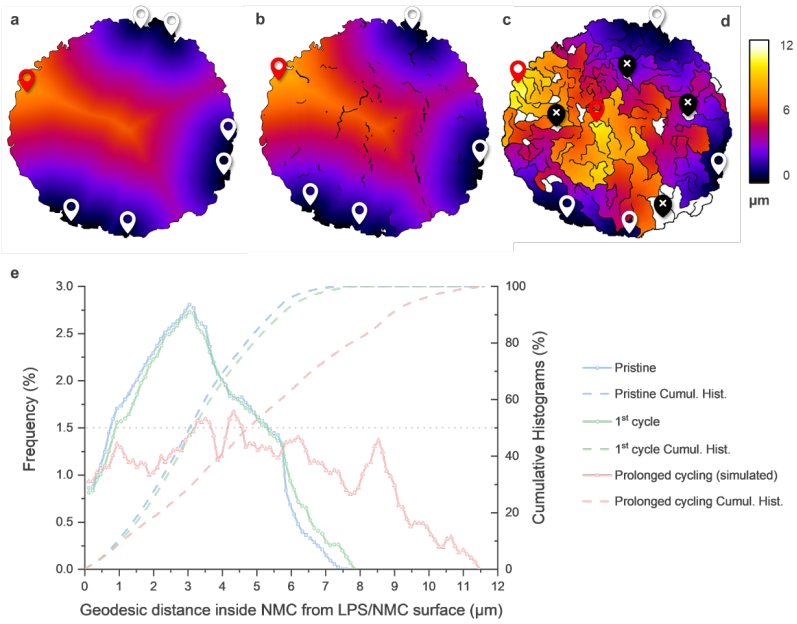

Figure 3: a, b, c) Geodesic distance maps of the lithium-ion paths inside NMC622 particles from the NMC-LPS interface (where lithium-ion transfer will occur, represented by a white marker) toward the inside of the secondary NMC particle (furthest distance represented by a red marker) from **Figure S7**. Calculations were made a) at a pristine state without internal fractures and LPS decohesion, b) after the first cycle with internal fractures and LPS decohesion and c) after simulated prolonged cycling with extended internal fractures and degraded LPS decohesion. d) The colour scale bar of the geodesic distance maps, e) the distribution of the distances and the cumulative percentage of the distances.

a supprimé: 4

Although this representation is only at the 2D level, ignoring the crystallographic orientation of each grain and thus the real ionic pathways inside the NMC, we can see that the path of lithium is elongated (**Figure 3a-c**). Fractures inside NMC will lengthen the lithium-ion solid

a supprimé: Figure 4

state diffusion throughout the NMC secondary particle. As the geodesic distance map colour observation may not be obvious, a distribution of the distances inside the particle, as well as its cumulative percentages, are presented in Figure 34e: the internal fracture will increase the lithium path inside the NMC particles as the lithium-ion will have to diffuse around them. The decohesion, on the other hand, will decrease the lithium-ion transfer at the NMC/LPS interface as less area connects the two, considering the same amount of lithium-ion exchanged (upper part of the NMC undergoing decohesion as shown in Figure 34b). At 50 % of the cumulative percentage (Figure 34e), the average distance difference is 0.125 µm between the pristine state and the first cycle while the maximum length increases from 7.5 to 7.9 µm. The lengthening of the path appears moderate but i) it only represents the first charge of the system, so this phenomenon will continue to increase and ii) it does not consider the real diffusion of lithium strictly perpendicular to the c-axis crystal orientation, here restricted to in-plane calculation. As batteries are targeted to undergo further cycles, fractures and interfacial decohesion will be even more pronounced, thus the lengthening lithium path and/or completely isolating NMC grains enhancing the ageing and worsening the electrochemical performance. Now we simulate a secondary particle after hundreds of cycles (where fractures are propagating everywhere and tend to block the diffusion), and the lithium-ion path lengthening becomes obvious (Figure 34c, Figure 34e, prolonged cycling (simulated)).

In Figure 34c, the fractures drastically increase the geodesic distances within the particle. In addition, fractures also fully disconnect primary particles (white area) which lithium-ion will no longer be able to access. The average distance rises from 3.1 to 4.9 µm from the pristine to the simulated prolonged cycling while the maximum length increases from 7.5 to 11.6 µm. Once again, these geodesic distance maps only consider the pathway of lithium-ion in the plan of cross-section. Still, such observation could be extrapolated to 3D microstructures of secondary NMC particles showing that better handling of the polycrystalline particles is key for solid-state batteries.

a supprimé: Figure 4

a supprimé: Figure 4

a supprimé: Figure 4

a supprimé: Figure 4

a supprimé: Figure 4

a supprimé: Figure 4

Another interesting observation is the heterogeneous displacements of various regions as shown in Figure 45 and **Figure S10**. Indeed, the composite electrode in solid-state batteries relies on a very complex 3D electrode architecture and suffers drastic chemo-mechanical degradation. We can somehow follow the dynamics mechanism behind the lithiation and delithiation and a so-called "re-organization" of the composite electrode.

a supprimé: Figure 5

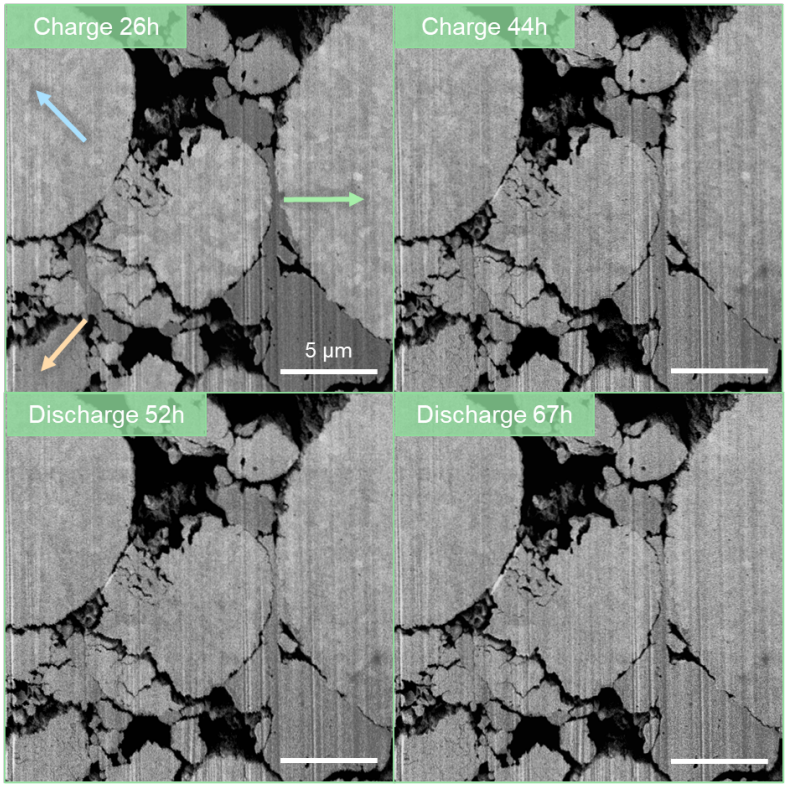

Figure 4: Heterogeneous displacements of various regions on secondary electron images. Each separate region's displacements are highlighted by arrows (**Movie 4 Heterogeneous Displacements**).

a supprimé: 5

In this figure, three regions composed of NMC particles and LPS can be distinguished by their displacements. A gap appears to grow between two NMCs of approximately 200 nm (the blue and green region, more visible in secondary images in Figure 45) while the NMC fractured from the shaping appears to split. This observation highlights that not only the active material is changing in a fixed environment through cycling, but agglomerates of active material and electrolyte move together. It is hard to attribute the displacement and their direction from a cross-section, but it is safe to say that the displacement of meaningful regions in the battery is caused by the overall lithiation/delithiation dynamics. It appears that some LPS-NMC contacts are still and that the entire block moves with the lithiation and delithiation processes, while some other LPS-NMC contacts are broken.

a supprimé: Figure 5

In this paper, we developed an advanced *operando* technique using a FIB-SEM to follow the dynamic changes occurring in composite electrodes of solid-state batteries. Although this technique "only" allows the study of cross-sections, morphological changes were observed during the first cycle. Due to the swelling of the active material during lithiation/delithiation, three regions composed of NMC and LPS were distinguished due to opposite displacements creating gaps in the cell. In addition, the study of the solid-state composite positive electrode with NMC622 and LPS showed different observations most likely to have a detrimental effect on the battery performance. Indeed, the fracturing of polycrystalline NMC has been observed at the grain boundaries as well as the decohesion of the NMC and LPS. Such morphological changes will increase the path of lithium-ion within the NMC as fracture will oppose the diffusion. Moreover, the decohesion creates a bottleneck for the lithium-ion extraction of the NMC as they become less and less numerous through cycling. The *operando* setup could also be improved as its stack pressure is rather weak (even if the literature tends to go to lower cycling pressure to be as close as possible to industrial protocol), increasing the impedance of the stack and thus limiting the cycling rate. Furthermore,

this 2D *operando* technique could be coupled to a 3D FIB-SEM tomography technique which could allow both 2D and 3D investigations. Lastly, the adaptation of this setup to a plasma FIB will allow more areas to be investigated as the FIB milling will no longer be the limiting factor.

AUTHOR INFORMATION

"The authors declare no competing financial interest."

ACKNOWLEDGMENT

This study would not have been possible without the financial support from Dr Sandrine Lyonnard and the Battery FOCUS group. I would also like to extend my deepest gratitude to Mr. Michel Boujard for the rapid solution and tuning of the solid-state cell. We also would like to thank Mr. Adrien Fauchier-Magnan for the supply of solid electrolytes. This work, carried out on the Platform for Nanocharacterisation (PFNC), was supported by the "Recherche Technologique de Base" and "France 2030 - ANR-22-PEEL-0014" programs of the French National Research Agency (ANR). Claire Villevieille thanks the ANR for the financial support through the grant OpInSolid.

ASSOCIATED CONTENT

Supporting Information:

Note 1 and Figure S1: Homemade half-cylindrical cell used in to assemble the FIB-SEM cell; Note 2 and Figure S2: *Operando* transfer box, assembly and electrochemical performance (OCV and EIS measurement) of the operando measurement; Figure S1; Image of the cross-section of the cell stack at the pristine state; Figure S2; Galvanostatic cycling of NMC composite electrode at ca. C/60 rate between 2.7 and 4.3 V vs. Li^+/Li; Note 3: Experiment performed to check the impact of beam damage during cycling**; Figure S3**; Pristine secondary electron images of a cross-section in LPS (255 MPa – 10 min); **Figure S4 and Figure S5**; SEM images highlighting beam damage at

a supprimé: 3

a supprimé: 4

a supprimé: 5

a supprimé: 6

a supprimé: 7

the mid-charge (26 h) and the end of the discharge (67 h); Note 4 and **Figure S6**; Causes of the NMC fracture dynamics**; Figure S7**; Illustration of the effect of decohesion and internal fracturing on the lithium-ion path inside the NMC particle between the pristine (left) and cycled state (right); **Figure S8**; Heterogeneous displacements of various regions; Movie 1 NMC fracturing; Movie 2 NMC fracturing and NMC-LPS decohesion; Movie 3 NMC-LPS decohesion; Movie 4 Heterogeneous Displacements; Materials and Methods section including Electrolyte synthesis, NMC providers, Electrochemical cycling condition, FIB-SEM preparation and data acquisition, Data pre-processing, Computational procedures - General quantification

a supprimé: 8

a supprimé: 9

a supprimé: 10

REFERENCES

(1) Golubkov, A. W.; Planteu, R.; Krohn, P.; Rasch, B.; Brunnsteiner, B.; Thaler, A.; Hacker, V. Thermal Runaway of Large Automotive Li-Ion Batteries. *RSC Adv.* **2018**, *8* (70), 40172–40186. https://doi.org/10.1039/C8RA06458J.

(2) Albertus, P.; Babinec, S.; Litzelman, S.; Newman, A. Status and Challenges in Enabling the Lithium Metal Electrode for High-Energy and Low-Cost Rechargeable Batteries. *Nat. Energy* **2018**, *3* (1), 16–21. https://doi.org/10.1038/s41560-017-0047-2.

(3) Janek, J.; Zeier, W. G. Challenges in Speeding up Solid-State Battery Development. *Nat. Energy* **2023**, *8* (3), 230–240. https://doi.org/10.1038/s41560-023-01208-9.

(4) Deiseroth, H.-J.; Kong, S.-T.; Eckert, H.; Vannahme, J.; Reiner, C.; Zaiß, T.; Schlosser, M. Li6PS5X: A Class of Crystalline Li-Rich Solids With an Unusually High Li+ Mobility. *Angew. Chem. Int. Ed.* **2008**, *47* (4), 755–758. https://doi.org/10.1002/anie.200703900.

(5) Kudu, Ö. U.; Famprikis, T.; Cretu, S.; Porcheron, B.; Salager, E.; Demortiere, A.; Courty, M.; Viallet, V.; Mercier, T. L.; Fleutot, B.; Braida, M.-D.; Masquelier, C. Structural Details in Li3PS4: Variety in Thiophosphate Building Blocks and Correlation to Ion Transport. *Energy Storage Mater.* **2022**, *44*, 168–179. https://doi.org/10.1016/j.ensm.2021.10.021.

(6) Perrenot, P.; Fauchier-Magnan, A.; Mirolo, M.; Lecarme, L.; Jouneau, P.-H.; Boulineau, A.; Bayle-Guillemaud, P.; Villevieille, C. Room-Temperature Sintering of Amorphous Thiophosphate Solid Electrolyte (Li3PS4): Coupling Morphological Evolution to Electrochemical Properties. *Adv. Funct. Mater.* **2023**, *n/a* (n/a), 2310739. https://doi.org/10.1002/adfm.202310739.

(7) Perrenot, P.; Bayle-Guillemaud, P.; Villevieille, C. Composite Electrode (LiNi0.6Mn0.2Co0.2O2) Engineering for Thiophosphate Solid-State Batteries: Morphological

Evolution and Electrochemical Properties. *ACS Energy Lett.* **2023**, 4957–4965. https://doi.org/10.1021/acsenergylett.3c01975.

(8) Athanasiou, C. E.; Liu, X.; Jin, M. Y.; Nimon, E.; Visco, S.; Lee, C.; Park, M.; Yun, J.; Padture, N. P.; Gao, H.; Sheldon, B. W. Rate-Dependent Deformation of Amorphous Sulfide Glass Electrolytes for Solid-State Batteries. *Cell Rep. Phys. Sci.* **2022**, *3* (4), 100845. https://doi.org/10.1016/j.xcrp.2022.100845.

(9) Baranowski, L. L.; Heveran, C. M.; Ferguson, V. L.; Stoldt, C. R. Multi-Scale Mechanical Behavior of the Li3PS4 Solid-Phase Electrolyte. *ACS Appl. Mater. Interfaces* **2016**, *8* (43), 29573–29579. https://doi.org/10.1021/acsami.6b06612.

(10) Ishidzu, K.; Oka, Y.; Nakamura, T. Lattice Volume Change during Charge/Discharge Reaction and Cycle Performance of Li[NixCoyMnz]O2. *Solid State Ion.* **2016**, *288*, 176–179. https://doi.org/10.1016/j.ssi.2016.01.009.

(11) Märker, K.; Reeves, P. J.; Xu, C.; Griffith, K. J.; Grey, C. P. Evolution of Structure and Lithium Dynamics in LiNi0.8Mn0.1Co0.1O2 (NMC811) Cathodes during Electrochemical Cycling. *Chem. Mater.* **2019**, *31* (7), 2545–2554. https://doi.org/10.1021/acs.chemmater.9b00140.

(12) Kroll, M.; Duchardt, M.; Karstens, S. L.; Schlabach, S.; Lange, F.; Hochstrasser, J.; Roling, B.; Tallarek, U. Sheet-Type All-Solid-State Batteries with Sulfidic Electrolytes: Analysis of Kinetic Limitations Based on a Cathode Morphology Study. *J. Power Sources* **2021**, *505*, 230064. https://doi.org/10.1016/j.jpowsour.2021.230064.

(13) Taillon, J. A.; Pellegrinelli, C.; Huang, Y.-L.; Wachsman, E. D.; Salamanca-Riba, L. G. Improving Microstructural Quantification in FIB/SEM Nanotomography. *Ultramicroscopy* **2018**, *184*, 24–38. https://doi.org/10.1016/j.ultramic.2017.07.017.

(14) Shi, T.; Zhang, Y.-Q.; Tu, Q.; Wang, Y.; Scott, M. C.; Ceder, G. Characterization of Mechanical Degradation in an All-Solid-State Battery Cathode. *J. Mater. Chem. A* **2020**, *8* (34), 17399–17404. https://doi.org/10.1039/D0TA06985J.

(15) Yadav, N. G.; Folastre, N.; Bolmont, M.; Jamali, A.; Morcrette, M.; Davoisne, C. Study of Failure Modes in Two Sulphide-Based Solid Electrolyte All-Solid-State Batteries via in Situ SEM. *J. Mater. Chem. A* **2022**, *10* (33), 17142–17155. https://doi.org/10.1039/D2TA01889F.

(16) Wu, X.; El Kazzi, M.; Villevieille, C. Surface and Morphological Investigation of the Electrode/Electrolyte Properties in an All-Solid-State Battery Using a Li2S-P2S5 Solid Electrolyte. *J. Electroceramics* **2017**, *38* (2–4), 207–214. https://doi.org/10.1007/s10832-017-0084-z.

(17) Lou, S.; Yu, Z.; Liu, Q.; Wang, H.; Chen, M.; Wang, J. Multi-Scale Imaging of Solid-State Battery Interfaces: From Atomic Scale to Macroscopic Scale. *Chem* **2020**, *6* (9), 2199–2218. https://doi.org/10.1016/j.chempr.2020.06.030.

(18) Cadiou, F.; Nguyen, T.-T.; Bettge, M.; Su, Z.; Ando, J.; Andrade, V. D.; Miller, D.; Demortière, A. Morphological Evolution of NMC Secondary Particles Through in Situ Electrochemical FIB/SEM Experiment., *arXiv preprint*, **2022**, 16. https://arxiv.org/abs/2208.00878

(19) Zhou, X.; Zhu, L.; Liu, Y. Operando Investigation of Energy Storage Material by FIB-SEM System. *Microsc. Microanal.* **2021**, *27* (S1), 440–442. https://doi.org/10.1017/S1431927621002087.

(20) Zhou, X.; Li, T.; Cui, Y.; Meyerson, M. L.; Mullins, C. B.; Liu, Y.; Zhu, L. In Situ Focused Ion Beam-Scanning Electron Microscope Study of Crack and Nanopore Formation in Germanium Particle During (De)Lithiation. *ACS Appl. Energy Mater.* **2019**, *2* (4), 2441–2446. https://doi.org/10.1021/acsaem.9b00380.

(21) Ryu, H.-H.; Park, K.-J.; Yoon, C. S.; Sun, Y.-K. Capacity Fading of Ni-Rich Li[NixCoyMn1–x–y]O2 ($0.6 \leq x \leq 0.95$) Cathodes for High-Energy-Density Lithium-Ion Batteries: Bulk or Surface Degradation? *Chem. Mater.* **2018**, *30* (3), 1155–1163. https://doi.org/10.1021/acs.chemmater.7b05269.

(22) Li, P.; Zhao, Y.; Shen, Y.; Bo, S.-H. Fracture Behavior in Battery Materials. *J. Phys. Energy* **2020**, *2* (2), 022002. https://doi.org/10.1088/2515-7655/ab83e1.

(23) Yari, S.; D'Haen, J.; Van Bael, M. K.; Hardy, A.; Safari, M. Fracture-Induced Aging Anomalies in LiNi0.6Mn0.2Co0.2O2 Electrodes. *Electrochem. Commun.* **2021**, *132*, 107134. https://doi.org/10.1016/j.elecom.2021.107134.

(24) Cadiou, F.; Nguyen, T.-T.; Bettge, M.; Su, Z.; Ando, J.; Andrade, V. D.; Miller, D.; Demortière, A. Morphological Evolution of NMC Secondary Particles Through in Situ Electrochemical FIB/SEM Experiment. *ArXiv Prepr.* **2022**, 16. https://doi.org/arXiv:2208.00878.

(25) Tsai, E. H. R.; Billaud, J.; Sanchez, D. F.; Ihli, J.; Odstrčil, M.; Holler, M.; Grolimund, D.; Villevieille, C.; Guizar-Sicairos, M. Correlated X-Ray 3D Ptychography and Diffraction Microscopy Visualize Links between Morphology and Crystal Structure of Lithium-Rich Cathode Materials. *iScience* **2019**, *11*, 356–365. https://doi.org/10.1016/j.isci.2018.12.028.

(26) Stavola, A. M.; Sun, X.; Guida, D. P.; Bruck, A. M.; Cao, D.; Okasinski, J. S.; Chuang, A. C.; Zhu, H.; Gallaway, J. W. Lithiation Gradients and Tortuosity Factors in Thick NMC111-Argyrodite Solid-State Cathodes. *ACS Energy Lett.* **2023**, *8* (2), 1273–1280. https://doi.org/10.1021/acsenergylett.2c02699.